Microstructural Evolution of Battery Electrodes During Calendering

Xuekun Lu[1,2,3,*], Sohrab R Daemi[1], Antonio Bertei[4], Matthew D.R. Kok[1], Kieran B O'Regan[3,5], Lara Rasha[1], Juyeon Park[2], Gareth Hinds[2], Emma Kendrick[3,5], Dan JL Brett[1,3], Paul R Shearing[1,3,*]

[1]Electrochemical Innovation Lab, Department of Chemical Engineering, University College London, London, WC1E 7JE, UK
[2]National Physical Laboratory, Hampton Road, Teddington, Middlesex, TW11 0LW, UK
[3]The Faraday Institution, Quad One, Harwell Science and Innovation Campus, Didcot, OX11 0RA, U.K.
[4]Department of Civil and Industrial Engineering, University of Pisa, Pisa, 56122, Italy
[5]School of Metallurgy and Materials, University of Birmingham, Birmingham B15 2TT, UK

Summary

Calendering is a crucial manufacturing process in the optimisation of battery performance and lifetime due to its significant effect on 3D electrode microstructure. By conducting an *in-situ* calendering experiment on lithium-ion battery cathodes using X-ray nano-computed tomography, here we show that the electrodes composed of large particles with a broad size distribution experience heterogeneous microstructural self-arrangement. At high C-rates, the performance is predominantly restricted by sluggish solid-state diffusion, which is exacerbated by calendering due to the increased microstructural and lithiation heterogeneity, leading to active material underutilisation. In contrast, electrodes consisting of small particles are structurally stable with more homogeneous deformation and a lower tortuosity, showing a much higher rated capacity that is less sensitive to calendering densification. Finally, the dependence of performance on the dual-variation of both porosity and electrode thickness is investigated to provide new insights into the microstructural optimisation for different applications in electrode manufacturing.

Keywords

Calendering, NMC cathodes, 3D microstructure, particle size, solid-state diffusion, heterogeneity, tortuosity, electrode thickness, image-based modelling, rated capacity

Introduction

Lithium-ion batteries (LiBs) have played a predominant role in energy storage for a range of applications from portable electronics and hybrid/electric vehicles to power grids, due to their unrivalled combination of high energy and power density[1]. Despite such success, technical challenges associated with durability, cost, performance and safety remain, and consequently substantial effort has been made by the scientific community to ameliorate these aspects from the perspectives of both electrode microstructural design and manufacturing[2-4]. Calendering is a critical step in the production of LiB as it reduces the electrode thickness compressively to achieve high energy density, which significantly determines the driving range and thus the market penetration of electric vehicles. Moreover, it greatly enhances contacts between the constituents of electrode to increase the electrical and thermal conductivity[5], which is particularly critical in thick electrodes that have a weak solid-phase percolation network[6,7]. Calendering is also known to affect the electrolyte wettability[8,9], which could be favoured by low calendering ratio (approx. 10%) by changing the pore structure of specific size ranges so that the long-term cycle stability and electrochemical performance was improved[10,11]. However, the rate capability of the LiB is known to drop with calendering process due to the increased lithium-ion mass transport resistance in the electrolyte[12,13]. Thus, a deep understanding of the calendering ratio and the resultant 3D microstructure of the electrode, and its interplay with electrochemical performance is required for rational electrode manufacturing.

Electrodes are often optimised to distinct microstructures for different applications assisted by calendering. For power-oriented cells, thin electrodes, small active particle size and high porosity are favoured structures to alleviate mass transport resistance[5,14] and facilitate reaction kinetics, as opposed to those required for high energy density cells,

---

* Corresponding author: Electrochemical Innovation Lab, Department of Chemical Engineering, UCL, London, WC1E 7JE, UK
 email: xuekun.lu@ucl.ac.uk (Xuekun Lu), p.shearing@ucl.ac.uk (Paul R Shearing)

as small particle size leads to high side-reaction rates and faster degradation whereas high porosity reduces the volumetric energy density. In simple terms, densifying the electrode introduces high energy density at the cost of power performance due to mass transport limitations and charge transfer capability. The reaction kinetics and mass transport dynamics are intertwined with both the 3D arrangement of all electrode constituents as well as the morphology of individual phases[15-17]. Rearrangement and deformation of active particles under incremental calendering could also affect the battery performance[18]. Understanding the effect of calendering on the microstructural evolution, the resultant electrochemical parameters and the battery performance are critical in rationalising manufacturing processes for battery design and optimisation. However, it is resource intensive to conduct a comprehensive experimental investigation to link the electrode microstructures with the corresponding calendering processes and their effect on the electrochemical performance.

Taking this into consideration, numerical approaches have been widely used to complement experimental work and provide additional insights into the influence of calendering during the manufacturing process. For instance, Lenze *et al.*[6] applied a pseudo-2D battery model to extract material parameters of electrodes subjected to different degrees of compression. Spherical particles were used to study the mechanical responses and porosity variation of the electrode under different calendering steps[19]. However, these studies were conducted based on simplified electrode geometries that were artificially-synthesised with spherical particles, ignoring the influence of particle shape and orientation on mass transport and electrochemical performance. More importantly, the carbon-binder domain (CBD), which is critical in determining the microstructural heterogeneities and electronic conductivity[20,21], especially under compression, was not taken into account. It is of great necessity to develop a model, based on a representative electrode microstructure, so that the effect of calendering on the microstructural heterogeneities and their electrochemical impact (e.g. non-uniform reaction and Li$^+$ ion transport) can be reliably assessed.

This necessitates non-destructive imaging techniques such as X-ray computed tomography (X-ray CT), which has been widely adopted as a valuable technique to image the 3D microstructure of battery materials[22,23]. However, a technical challenge in imaging electrode materials is the ability to distinguish micro-pores from CBD due to the similarity of the X-ray attenuation coefficient between air and carbon. The contrast is further reduced in the presence of embedded highly attenuating active materials. To circumvent this, various numerical algorithms based on different physical models have been used to generate stochastic CBD phases that are then incorporated into the reconstructed electrode[17,24-26], which casts doubt on the representativeness of the structure. To reconstruct the full microstructure of the NMC electrode, a novel dual-scan superimposition (DSS) technique has been developed as described elsewhere[27,28] to resolve the low-absorption carbon-binder and nano-pore phases.

Among the material parameters that are affected by the calendering process, pore phase tortuosity plays a critical role in determining the rate capability[29,30]. It is dependent on both the porosity and the morphology of the solid materials. While some studies have discussed the anisotropic tortuosity related to the particle shape, the lack of resolution of the CBD due to the aforementioned technical challenge means that the pore phase is misrepresented and the influence of active particles on Li$^+$ ion transport is underestimated[31,32]. Linking the porosity and pore network tortuosity to the incremental calendering steps with the inclusion of CBD on the same sample is particularly critical in guiding microstructure control for desired performance. This microstructural parameterisation is the key information required by control-oriented battery models[33,34] used in battery management systems (BMSs) for online diagnosis and prognosis[35,36].

In this study, we use *in-situ* X-ray nano-computed tomography to monitor different microstructural responses during the calendering process for LiNi$_x$Mn$_y$Co$_z$O$_2$ (NMC) electrodes constituted of large and small active particles respectively. Assisted by the DSS technique previously developed by the authors to resolve the CBD phase and active material/electrolyte interface at nanoscale, key material metrics such as porosity, tortuosity, pore size distribution and solid/electrolyte interfacial area are quantified. High-fidelity fully microstructure-resolved battery models are then employed to investigate the interplay between the resultant electrochemical performance and the 3D microstructure at incremental calendering steps. Finally, a correlation between cell performance and the dual-variation of porosity and electrode thickness is conducted to underpin the microstructural design and manufacturing of battery electrode.

Results and discussion

Microstructural evolution as a function of calendering process

To replicate the calendering densification process in electrode manufacturing, a bespoke nano-mechanical test stage was integrated into the X-ray nano-CT system[37,38]. The stage fixture and experiment setup are shown in Fig. 1a and b. Two samples, namely the as-prepared electrode (i.e. NMC + CBD, Fig. 1c) and stand-alone CBD (Fig. 1d) are compressed, scanned and reconstructed separately, followed by DSS[27,28] to reconstruct the full 3D microstructure of the electrode, including the CBD. More details about the methodology and DSS technique can be found in the *Experimental* section. Fig. 1e-g shows the microstructural evolution of an electrode composed of large particles (AM_L) at incremental calendering steps. Apart from the decrease of pore size, particle deformation and rotation (Fig. 1g, h, details of the colour-coded cylinders in (h) are discussed later) are observed as well, which is consistent with the previous speculation[18]. This is in contrast with the electrode consisting of smaller active material particles (AM_S), which is displayed in Fig. 1i-k with the non-particle domain overlaid by a colourmap showing the change of inter-particle distance as a function of progressive calendering. Unlike AM_L, free particle movement and localised deformation are not evident in AM_S, possibly as a result of the more stable structure formed by the small particle size. Direct comparison of the particle size distribution is intuitively visualised in Fig. 1l, assisted by the 3D distribution of the particles colour-coded proportionally to the actual size. The mean particle size D_{mean} for AM_L and AM_S is 7.3 μm (STD 3.1 μm) and 5.2 μm (STD 1.8 μm) respectively, with the former having a broader size distribution. The distribution of diffusion time constant of the particles for AM_L and AM_S is shown in Figure S1, which indicates that 50% of the particles in AM_S can reach a maximum C-rate of 5C (C_{50}) and 90% of them can reach 1.8C (C_{90}), much higher compared to those in AM_L (C_{50} = 3C and C_{90} = 0.8C).
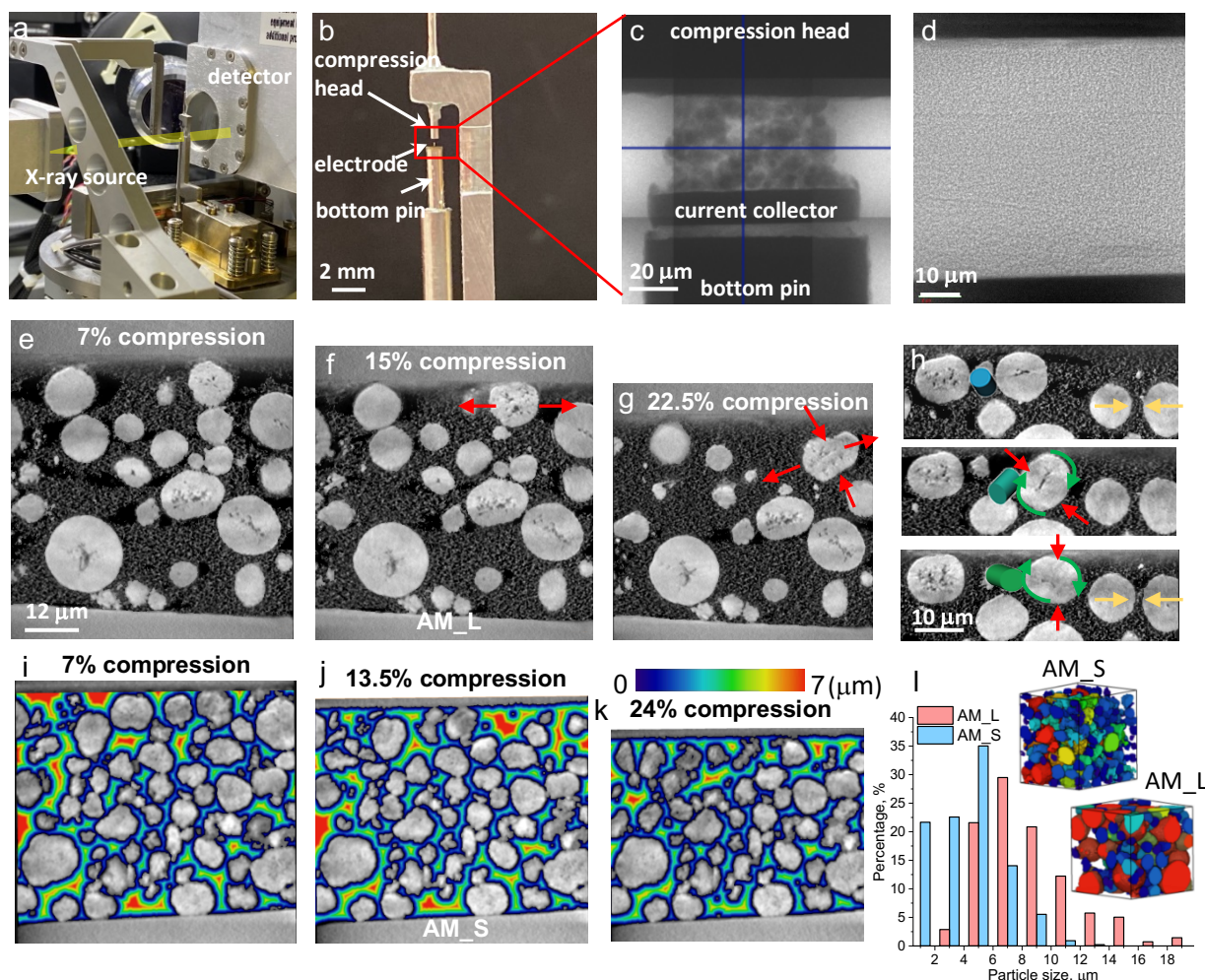

Fig. 1 *In-situ* electrode calendering experiment using X-ray nano-CT and the resultant microstructural evolution. (a) Experimental set-up showing the relative position of the X-ray source, loading stage and detector; (b) alignment of the electrode pillar under compression pinhead; (c) X-ray radiograph of the electrode before compression; (d) X-ray radiograph showing a stand-alone CBD (no NMC particles); (e)-(g) reconstructed virtual slices showing the microstructural change of the AM_L electrode under incremental compression, following a DSS procedure to include the deformation of CBD. Red arrows indicate the particle deformation; (h) structural self-arrangement (from top to bottom) via particle rotation and deformation. Details of the cylinders to characterise particle orientation are

introduced later; (i)-(k) reconstructed virtual slices overlaid with colourmap showing the change of the inter-particle gap under incremental calendering of the AM_S electrode; (l) comparison of the particle size distribution between AM_S and AM_L. The standard deviation for AM_S and AM_L is 1.8 and 3.1 μm respectively. The insets display the morphology of the colour-coded particles, highlighting the average size difference. Subset (a), (b) and (h) are reproduced from the previous work[27].

To further highlight the particle size-related microstructural evolution under calendering, detailed particle morphology analysis has been conducted (Fig. 2), by extracting the eigenvalues and eigenvectors of the moments of inertia matrix for each of the individual NMC particles[39]. The size, orientation (corresponding to the orientation of the largest eigenvector of the particle geometry) and shape (described here as "ovality", equal to 1 - b/a; b/a is the ratio of the shortest to longest axis of an equivalent ellipsoid) are represented by the size, axis orientation and colour (blue to red: low to high ovality) of the cylinders for individual particles in Fig. 2a (AM_L) and Fig. 2b (AM_S). By comparing the two electrodes, it is shown that NMC particles in AM_S are generally smaller and more elliptical. An exemplary particle that experiences rotation and compressive deformation (evidenced by the change of colour) simultaneously is highlighted in Fig. 1h. It finally settles down with the long axis aligning parallel to the horizontal direction, impeding ion transport. To illustrate this, a comparative study of three types of electrodes with differently oriented particles and shapes is conducted and their impact on flow streamlines and flux are presented (Figure S2). This adverse effect could be amplified in high mass loading cathodes when heavily calendered. The particle rotation and deformation could also exert a lateral compressive force on adjacent particles (yellow arrows). By applying the morphological analysis to both types of electrodes, a distinctly different response to the calendering is revealed by comparing the shape distributions of the particles before and after calendering. Firstly, the ovality distribution of AM_L particles is fairly wide (Fig. 2c), suggesting a high microstructural heterogeneity compared to AM_S particles, which show a narrower and preferential shape distribution with the particle ovality around 0.7 (Fig. 2d). Secondly, the random fluctuation of shape change (red columns) implies that AM_L was undergoing macroscopic self-arrangement, with some particles becoming more spherical at the expense of less elongated ones and vice versa. This phenomenon occurred concurrently with inter-particle sliding and rolling, as shown in Fig. 1h. This observation is in good agreement with the previous speculation that active particles undergo rearrangement, deformation and finally fracture under incremental calendering process[18]. However, the random fluctuation of the shape change with small magnitude also indicates that the particle deformation is heterogeneous and mild (i.e. each region behaves differently).

In comparison, the calendered AM_S displays a remarkable spike at 0.75, primarily coming from the less (0.6) and more elongated (0.85) particles, with approx. 60% of particles falling within the ovality range between 0.65 to 0.8. This implies that particles deformed collectively to form a preferential orientation and shape, possibly due to the high lateral constraints from neighbouring particles as a consequence of high specific area and small inter-particle gap. The orientation distributions before and after calendering for AM_L and AM_S are plotted in Fig. 2e, f and Fig. 2g, h respectively (for the out-of-plane angle, 0° means long axis of the particle aligns vertically to the current collector), with the symbol colour and size corresponding to the actual particle size. It is intuitive to see that the particles are randomly distributed in AM_L without preferential alignment, even after calendering. The particle represented by the yellow symbol aligned more towards the horizontal plane but the in-plane orientation stayed unchanged, meaning a vertical rotation. Some other particles behave differently. Nonetheless, AM_S manifests a strong preferential arrangement of the particles even before calendering, evidenced by the clusters around 90° and 270°. After calendering, there is a tendency that particles initially located at the inner circle move outward (i.e. orienting more horizontally) and the preferential orientation becomes more pronounced, in accordance with Fig. 2d.
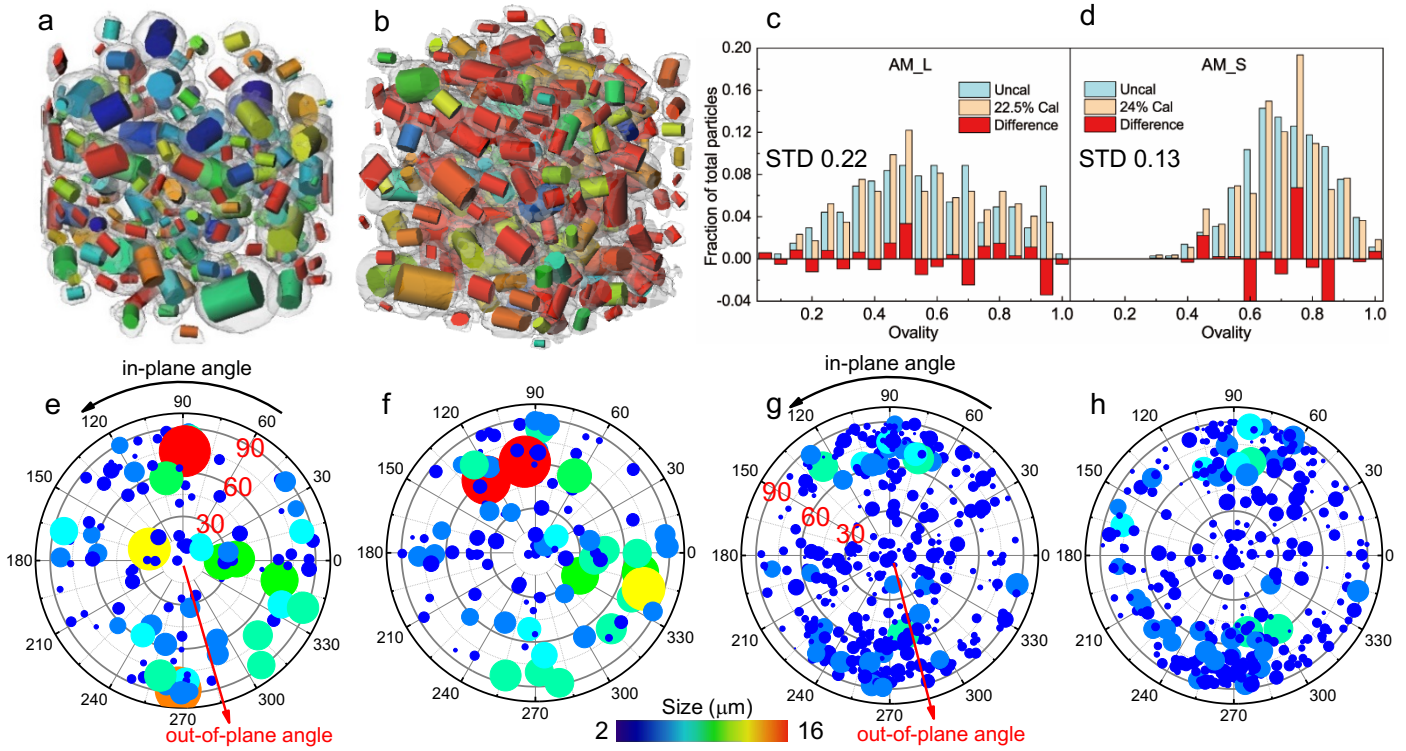
Fig. 2 Shape and orientation of NMC particles under calendering. (a)-(b) Representation of individual NMC particles by cylinders with size and colour corresponding to the particle size and ovality (blue to red: spherical to flake) for AM_L and AM_S respectively. An exemplary particle that experienced rotation and deformation under incremental compression is shown in Fig. 1h. (c)-(d) Fractional particle distribution as a function of particle ovality for two types of electrodes. The red bars indicate the change before and after calendering at each ovality level; (e), (f) and (g), (h) representing the orientation distribution before, after calendering for AM_L and AM_S electrode respectively. The size and colour of the symbols correspond to the actual particle size.

Apart from the NMC particles, pore phase also shows distinct behaviour between the two electrodes under calendering. Fig. 3a-d compares the changes of inter-particle gap size and percolated network before and after calendering using colour-coded skeletons. It shows that the inter-particle distance is significantly larger in uncalendered AM_L than AM_S, whereas AM_S displays more complex interconnections of the pore phase. The broad range of the gap size in AM_L is attributed to the wide distribution of particle size and shape, affecting the homogeneity of the CBD and pore size distribution, as opposed to AM_S, where the microstructure is more homogeneous. Pore connectivity analysis is conducted for both electrodes before and after calendering (Figure S3). The results show that the AM_S has two times more pore segments and junction nodes than AM_L. Calendering affects the pore percolation evenly in AM_S, whereas it mainly reduces the junction nodes of high coordination number in AM_L, which is critical for the global connectivity considering the coarse pore structure in AM_L. An exemplary region is highlighted (dashed circle) in Fig. 3a showing the loss of pore percolation. This is consistent with the previous observation that AM_L experiences structure re-arrangement associated with particle movement during calendering. However, mass transport in pore is less affected in AM_S due to the substantial percolated pathways distributed homogeneously, confirmed by the tortuosity measurement (discuss later). This is conducive to an even distribution of the compressive stress and strain across the whole electrode. Fig. 3e-h shows the results of liquid permeability simulation (see *Experimental* section for more details) performed on the 3D pore structures before and after calendering, with the colour-coded streamlines showing the flow trajectory and normalised fluid velocity. Whilst permeability does not directly influence the cell in operation, it dictates the wetting of electrolyte during cell construction, and moreover provides a valuable insight into microstructure heterogeneity and its influence on pore phase transport phenomena[11]. Based on the velocity distribution of the uncalendered electrodes, AM_L shows an overall slower mass transport, with approximately 70% of the permeability of the AM_S electrode due to the lower initial porosity. However, the permeability of the calendered AM_S is lower than that of the calendered AM_L, which

suggests that electrolyte wetting is hindered by the high surface area and viscous resistance and hence would take longer in the compressed electrode with fine particles.
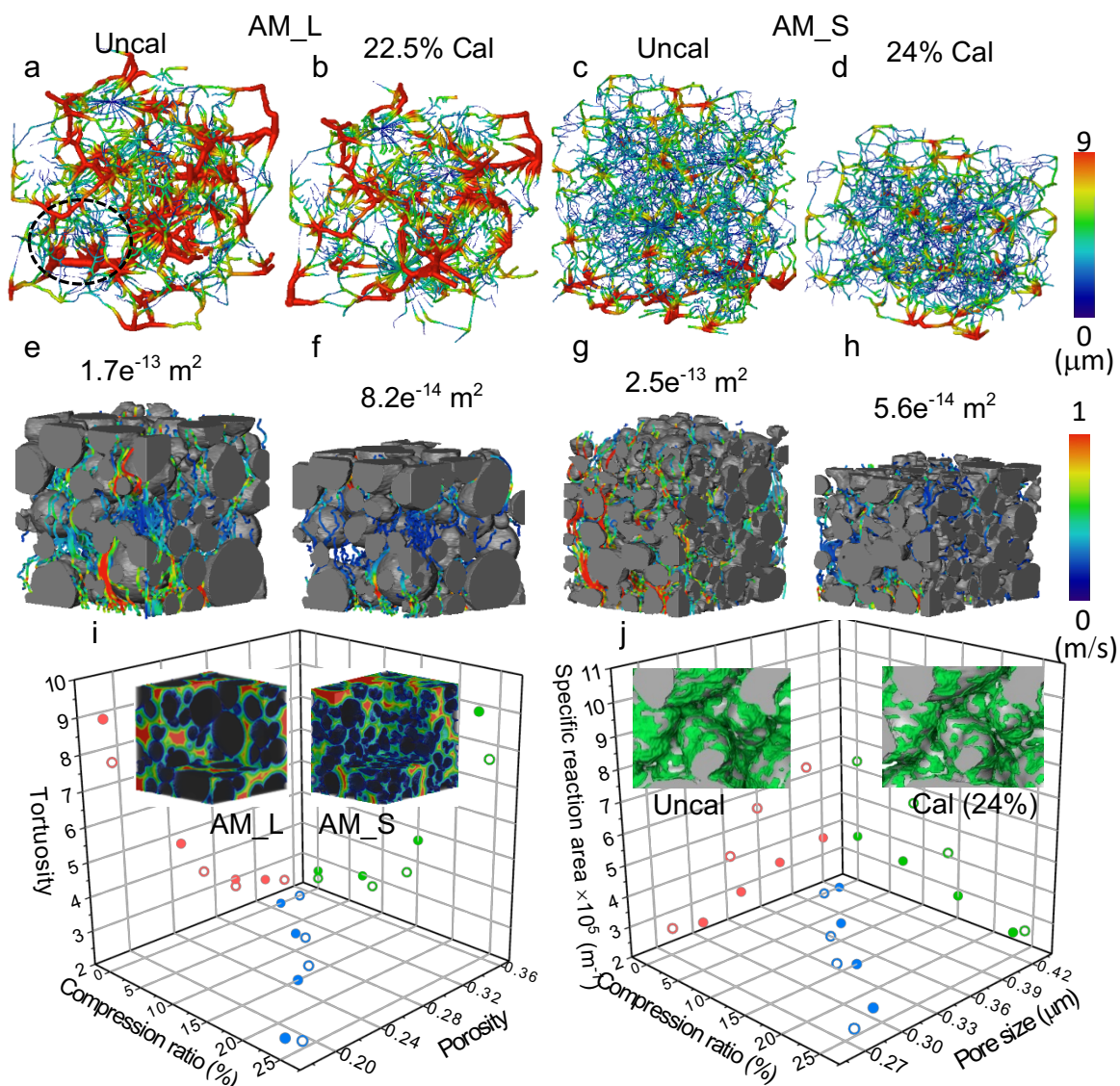

Fig. 3 Morphological evolution of the pore phase under calendering. Colour-coded skeletons are used to represent the inter-particle gap size for (a) uncalendered and (b) 22.5% calendered AM_L electrode, (c) uncalendered and (d) 24% calendered AM_S electrode; (e)-(h) electrolyte permeability simulation of the pore phase of the respective microstructures, with colour-coded streamlines showing the relative (normalised) fluid velocity; dependence of (i) tortuosity and porosity, (j) specific reaction area and average pore size on the compression ratio. Insets compare the size distribution of inter-particle gap in (i) and compare the spatial distribution of reaction area before/after calendering in AM_S in (j). Measurements in (e) – (j) use three-phase electrode. Solid and hollow symbols represent AM_L and AM_S respectively. The dashed circle in (a) highlights the loss of pore connectivity under calendering.

Fig. 3i summarises the variation of porosity and tortuosity as a function of the compression ratio based on fully reconstructed electrodes (3 phases), with the inset showing the inter-particle gap. Tortuosity here is a material parameter that represents the Li$^+$ ion transport resistance arising from the convoluted morphology of the pore phase (Equation. S1-S3). It is found that the trend of porosity reduction is similar between AM_L (solid symbols) and AM_S (hollow symbols), although AM_S has slightly higher overall porosity. Furthermore, for a given porosity, AM_L shows a higher pore phase tortuosity than AM_S, especially at high calendering ratios, as a consequence of the heterogeneous pore structure that is more sensitive to the percolation loss subject to calendering. It is worth emphasising the importance of including CBD in the tortuosity measurement otherwise the effect of microstructural heterogeneity is significantly weakened. To substantiate this, two-phase (active particle and pore) and three-phase (particle, pore and CBD) tortuosity is compared to prove that the CBD plays a determining role in mass transport properties (Figure S4). The influence of calendering on reaction kinetics is shown in Fig. 3j. AM_S possesses a much

higher specific reaction area than AM_L, as a consequence of a smaller particle size and homogeneous microstructure. However, this in turn yields a greater loss of surface area under calendering, as shown in Fig. 3j (green circles).

In a short summary, AM_L experiences structure re-arrangement under calendering, accompanied by heterogeneous particle movement, deformation and random orientation, as opposed to AM_S, which has a stable framework due to the smaller and narrower distribution of particle size (STD 1.8 vs. 3.1 μm), and thus the particles react more uniformly to the external compression, leading to a preferential distribution of the particle shape and orientation. Despite the large inter-particle gap, AM_L experiences critical loss of pore connectivity and rapid rise of tortuosity compared to AM_S, the fine structure of which however is disadvantageous in electrolyte wetting due to the high surface area and viscous effect.

Electrochemical performance as a function of the calendering process

Half cell (i.e. NMC622 vs. Li metal) modelling (detailed parameters in Table S1) using the reconstructed 3D microstructures of the uncalendered and calendered electrodes was conducted to investigate the influence of calendering on the electrochemical performance. Fig. 4a-c presents the spatial distribution of state-of-lithiation (SoL) for AM_L at 60% degree-of-discharge (DoD) under different calendering and discharge conditions, in comparison to those for AM_S (Fig. 4d-f). It is observed that lithiation of the active particles in AM_L is markedly heterogeneous, with the large particles lithiating to a lesser degree than the small ones, due to a longer solid diffusion pathway. Quantitative investigation shows that in AM_L, a 11 μm particle is intercalated 14% less than a 5 um particle at 3 C and becomes more distinct (18%) at 5C (Table S2), with the former having 1.5 to 2 times larger intra-particle variation of SoL. Consequently, a substantial fraction of active material particles in AM_L is under-utilised at the end of discharge, leading to capacity loss. However, this is not observed in AM_S as the particles are much smaller with a narrower size distribution (STD 1.8 μm). Nonetheless, this non-uniform inter-particle SoL distribution is not observed at low C-rates (Figure S5), since the relative rate between solid-state mass transport and the surface reaction kinetics has a determining effect on the electrochemical performance, particularly in electrodes composed of large active particles.

Comparing Fig. 4a and b, the intra-particle lithiation gradient develops with the calendering steps, featured by a slightly higher lithium concentration layer at the surface and becoming more pronounced at 5C (Fig. 4c). The SoL profiles from the particle surface to the core are compared between two particles (11 μm vs. 5 μm) extracted from Fig. 4a, b and c. (Figure S6). It is noticed that calendering has less influence of the lithiation behaviour in the small particle than in the larger one, mainly at the particle surface, where the average SoL increases by 0.04 at 22.5% calendering at 3C, with 13.5% rise of surface-to-core SoL gradient. Discharge at 5C increases the SoL gradient by 67% and 64% in small and large particle respectively. Particularly, it is noted that the curvature of the exponential SoL profile differs between C-rates but is independent of the particle size. The other disadvantage of using large active particles for high current applications is the high activation overpotential η_{act}, which represents the voltage loss required to drive the charge transfer process at certain rate due to slow reaction kinetics at the particle/electrolyte interface, either due to high reaction energy barrier or low reaction area. AM_L shows a much higher η_{act} (Fig. 4g-i) in comparison to AM_S (Fig. 4j-l) partly because of the much lower specific reactive area in AM_L due to the particle size effect (Fig. 3j). Furthermore, slow solid diffusion dynamics in AM_L particles causes a severe Li accumulation at the surface, which in turn is detrimental to the charge transfer kinetics due to the lowered exchange current density[40]. A non-uniform distribution of the activation overpotential in AM_L is observed, and is thought to arise from the microstructural heterogeneity and reflect the uneven reaction activity. This could cause local stress concentration (cracking)[41], structural transformation (from a layered structure to a defective spinel structure) and transition metal dissolution[42], especially for Ni-rich cathodes, accelerating degradation and reducing cycle life.

The corresponding electrolyte salt concentration distribution C_{ey} for the two electrodes is shown in Fig. 4m-o (AM_L) and Fig. 4p-r (AM_S). Compared with the uncalendered AM_L, a 2.5-fold increase of the C_{ey} gradient is observed in the 22.5% calendered electrode, and it increases further by 180% from 3C to 5C discharge condition. AM_S shows 25% to 30% lower gradient of C_{ey} compared to the counterparts of AM_L. However, Li$^+$ ion transport is not the primary performance-limiting factor for the two electrodes as the electrolyte concentration is far from depletion in the proximity of the current collector, due to the relatively low electrode thickness (approx. 35 μm after calendering) and moderate mass loading (NMC volume fraction approx. 0.45). Fig. 4s-u and Fig. 4v-x compare the Li$^+$ ion flux distribution

in the pore domain for AM_L and AM_S, respectively. As is presented from the 3D pore morphology analysis (Fig. 3a, b and i), the heterogeneous microstructure of AM_L leads to a non-uniform percolated pore network and ionic transport resistance, which becomes worse after calendering and causes high current flux locally. This could create large ohmic heating accumulated during battery cycling or under high C-rate operating conditions. Apart from ohmic heat, the decrease of active electrode/electrolyte interfacial area by calendering could aggravate the local temperature rise due to more reaction heat generated per unit surface area. The ohmic and reaction heat combined lead to temperature heterogeneity across the electrode and ultimately cause thermal stress-induced structural failure[43,44] and early thermal runaway[4]. On the other hand, high temperature facilitates the mass transport dynamics and kinetically favours the exchange current density, which are conducive to improved rate capability and could inherently mitigate the performance heterogeneity[35]. In long-term operation, uniform heat distribution and temperature control via microstructural design and calendering are still critical to suppress side reactions and prolong battery cycle life.
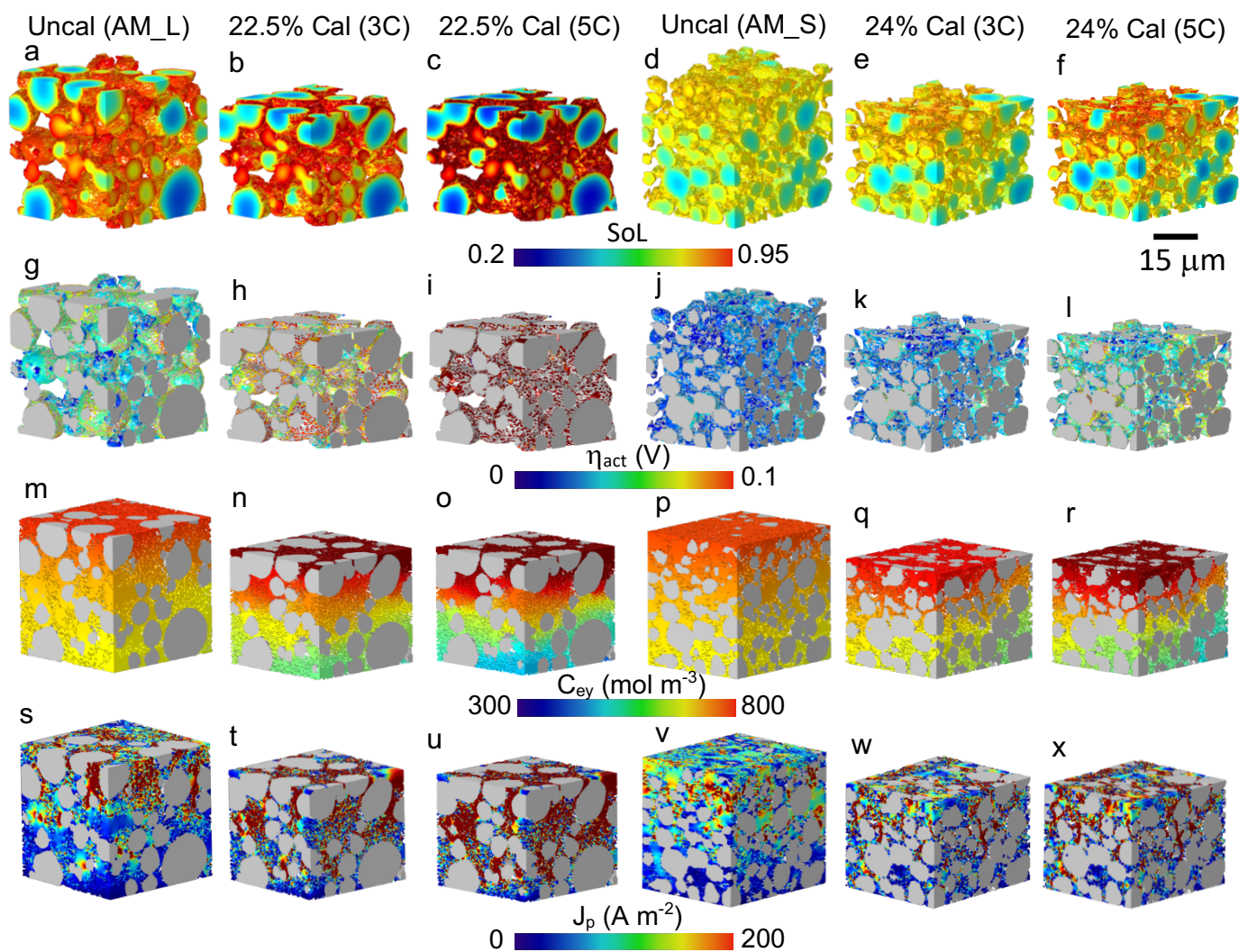

Fig. 4 Electrochemical parameters obtained at 60% DoD, at discharge rates of 3C and 5C with incremental calendering. (a)-(c) and (d)-(f) Spatial distribution of SoL in AM_L and AM_S; (g)-(i) and (j)-(l) spatial distribution of activation overpotential η_{act} at the active particle/electrolyte reacting interface in AM_L and AM_S; (m)-(o) and (p)-(r) spatial distribution of electrolyte concentration C_{ey} in AM_L and AM_S; (s)-(u) and (v)-(x) spatial distribution of Li$^+$ ion flux J_p in AM_L and AM_S. The separator side is at the top.

The simulated electrochemical performance of the uncalendered and calendered electrodes is compared in Fig. 5a-b (AM_L) and Fig. 5c-d (AM_S). Inspecting the discharge curves, the rated capacity of uncalendered AM_L decays more rapidly than in uncalendered AM_S. AM_L is unable to retain 80% of total capacity above 3C, in contrast to AM_S (which does so even at 5C). As the porosity is above 30% for both uncalendered electrodes and no obvious depletion of the electrolyte is observed throughout the thickness (Fig. 4a and d), this disparity of rate performance is speculated

to largely originate from the solid-state diffusion, since AM_S has much higher C_{50} and C_{90} than AM_L (5C vs. 3C for C_{50} and 1.8C vs. 0.8C for C_{90}), as discussed in the context of Fig. 1l. Faster reaction kinetics that are related to the particle size and specific reaction area in AM_S also lead to a better rate capability. Furthermore, little performance difference is observed between the uncalendered and 24% calendered AM_S, whereas the performance of 22.5% calendered AM_L shows a more significant drop. As the solid-state diffusion rate is not markedly dependent on calendering (Figure S7), the different responses before and after the process primarily depend on the reaction kinetics that are in turn related to the loss of specific reaction area due to the reduction of porosity and connectivity. AM_L is observed to be more susceptible to this in that calendering can exacerbate the solid-diffusion resistance further. Note that even at 0.2C, when polarisation from the solid-state diffusion and Li$^+$ ion transport is small, calendered AM_L exhibits an inferior specific capacity to the uncalendered sample, confirming the impact of porosity loss on reaction kinetics. To further corroborate this, comparison of the performance of a high mass loading NMC622 electrode (AM_LH, 2 mAh cm^{-2} vs. AM_L, 1.5 mAh cm^{-2}) with similar particle size distribution (hence comparable solid-state diffusion resistance) is made (Fig. 5e and f). The simulated performance is in good agreement with the experimental results (solid lines), except for a noticeable discrepancy at 5C. Uncalendered AM_LH shows a slightly lower discharge capacity than AM_L, likely due to a lower porosity, as indicated in Table 1. The similar trend of capacity decrease between uncalendered AM_L, AM_LH and 18% calendering AM_LH across the C-rates proves that the only invariable, namely the particle size distribution, is key in determining the macroscopic performance, when the Li$^+$ ion transport is not a limiting factor. 18% calendered AM_LH shows a reduced capacity drop compared to the 22.5% calendered AM_L, which is attributed to a lower activation overpotential due to a higher porosity. The average voltage V_{avg}, which is an important metric in evaluating the power performance of the battery, is plotted as a function of C-rates for the uncalendered and calendered AM_L and AM_S electrode in Figure S8. AM_L shows a much faster drop rate of the V_{avg} compared with AM_S, in which the V_{avg} is relatively stable until 2C. AM_S can maintain the V_{avg} above 3.75 V at 5C in comparison to AM_L (3.706 V for uncalendered and 3.656 V for calenderd). This also suggests that the power performance of AM_L is much more susceptible to calendering.

The disparity of electrochemical performance and response to the calendering between AM_L and AM_S can be further explained by investigating the distribution of the electrochemical variables η_{act} (Fig. 5g) and SoL (Fig. 5h and i) at 60% DoD and, 3C discharge. It is clear that the average η_{act} rises drastically with the incremental calendering steps for AM_L, while η_{act} for AM_S is less sensitive to calendering. More importantly, the η_{act} plot is more fluctuated across the electrode thickness for AM_L, with a large in-plane variation, reflected by shaded zone for each curve, implying a strong correlation between the pore and reaction heterogeneity caused by the broad particle size distribution, as explained later. This microstructural inhomogeneity not only undermines the electrochemical performance but could also accelerate structural and chemical degradation of the electrode and cell. In-plane performance inhomogeneity is also found from the SoL distribution in AM_L (Fig. 5h). A smoother SoL curve and less in-plane variation are observed for AM_S (Fig. 5i). Note that as the calendering proceeds, a mild SoL gradient starts to develop from the separator to the current collector, implying an increasing impact of Li$^+$ ion transport on the reaction kinetics, but the extent is too small to be predominant.

Characteristic peaks (P_1, P_2), that correspond to locally high particle lithiation, can be identified in the SoL plot and linked to the specific local microstructure. Only P_1 appears for the calendered AM_S and no peak is observed for the uncalendered AM_S because of the uniform lithiation. As a consequence of incremental compression, P_1 and P_2 move closer and partially overlap at 22.5% calendering, suggesting the coalescence of two distinct types of structural configuration. The magnitude of the P_1 peak is identical for the uncalendered and 15% calendered AM_L curves, whereas it drops slightly for 22.5% calendering. This implies that under heavy calendering, the resultant loss of active area in AM_L, particularly in the vicinity of the separator, limits the utilisation of local active materials, leading to an exaggerated uneven lithiation profile (large SoL variation shown as a green dashed line), and thus the lithiation in this region propagates deeper into the electrode, as evidenced by the rise of P_2 peak. In contrast, AM_S is not as susceptible to the loss of reaction area as AM_L during calendering, which consequently favours the reaction in the proximity of the separator due to the higher electrolyte concentration (Fig. 4f and Fig. 4r) that facilitates the charge transfer process.
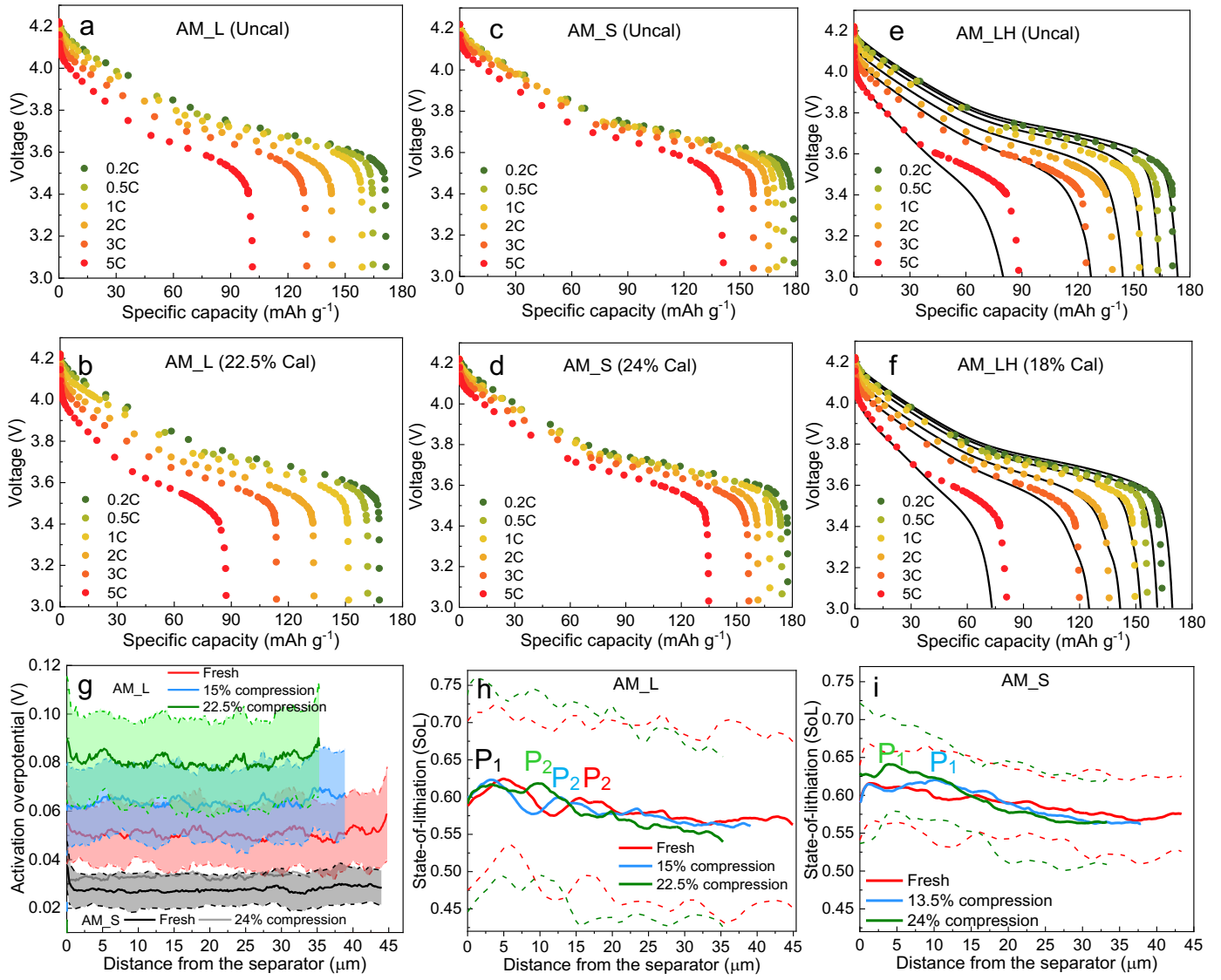
Fig. 5 Correlation between the global and local electrochemical performance. (a)-(d) Comparison of the simulated discharge performance between AM_L and AM_S before and after calendering. AM_LH in (e) and (f) refers to an electrode composed of large particles with heavier mass loading than AM_L (2 mAh cm⁻² vs. 1.5 mAh cm⁻²) and the solid lines represent the experimental results; (g) comparison of the η_{act} distribution (solid lines) and its in-plane variation (shaded area) as a function of the distance from the separator under different calendering conditions; (h) and (i) comparison of the SoL distribution (solid lines) and its in-plane variation (dashed lines) as a function of the distance from the separator under different calendering conditions, with P1 and P2 indicating two characteristic peaks associated with the same local microstructure.

Table 1 Microstructural parameters for the selected electrodes

	Areal capacity (mAh cm⁻²)	AM Volume Fraction	Thickness (µm)	Porosity
AM_L (Uncal)	1.5	0.46	45	0.325
AM_L (22.5 % Cal)	1.5	0.52	35	0.188
AM_LH (Uncal)	2	0.57	48	0.286
AM_LH (18% Cal)	2	0.62	39	0.217
AM_L1.5 (22.5% Cal)	2.25	0.52	53	0.188
AM_L2 (22.5% Cal)	3	0.52	70	0.188
AM_S (Uncal)	1.5	0.45	43	0.354
AM_S (24% Cal)	1.5	0.50	33	0.195
AM_S1.5 (24% Cal)	2.25	0.50	50	0.195
AM_S2 (24% Cal)	3	0.50	66	0.195

10

Understanding sub-micron reaction kinetics and heterogeneity

To provide manufacturing solutions for electrode design and optimisation, it is critical to understand the competition between reaction kinetics and mass transport dynamics at a sub-micron length scale that determines the macroscopic performance (Fig. 6). Fig. 6g compares the simulated discharge performance of the 22.5% calendered AM_L with three distinct properties (1) as-prepared electrode; (2) faster solid-state diffusion Ds_f; (3) faster reaction kinetics Rk_f (i.e. larger reaction rate constant j_{00_f}). Ds_f and j_{00_f} can be found in Figure S7 and Table 1, respectively.

It is observed from the discharge curve that having faster reaction kinetics improves the operating voltage across the whole discharge window, but the maximum specific capacity does not vary considerably from the initial performance. In contrast, faster solid-state diffusion substantially increases the operating voltage and extends the capacity. This confirms that, even though AM_L has a low specific reaction area, it is the solid-state diffusion that predominantly restricts the cell performance under high-rate conditions. To better understand this, the spatial distribution of SoL and η_{act} corresponding to the transient state on the vertical dashed line, are visualised in Fig. 6a-f respectively. By correlating SoL (Fig. 6a) and η_{act} (Fig. 6d) at the particle/electrolyte interface, co-localisation of low η_{act} and high SoL regions is observed, either at the locations where there is a large pore (indicated by black arrows) leading to a high Li$^+$ ion influx, or at the surface of small particles (indicated by the blue arrow). This originates from a decreased equilibrium lithiation potential V_{eq} that is dependent on the SoL ($\eta_{act} = \mu_p - \mu_e + V_{eq}(SoL)$, μ_p: potential in the electrolyte; μ_e: potential in electron-conducting phases).

The non-uniform pore size distribution around a single particle, introduced by improper mixing or drying, and aggravated by a heterogeneous particle size distribution, inevitably results in an uneven intra-particle reaction activity thereby likely to crack the particles due to the accumulation of mechanical and thermal stresses that are closely associated with the capacity loss and premature failure[41]. In addition, small particles are more lithiated and thus have a much lower V_{eq} (up to -0.04 V difference) than the larger particles (black arrows in Fig. 6j). This impedes further lithiation of small particles; therefore, lithiation has to proceed on large particles at the expenses of a higher activation overpotential η_{act}, causing inter-particle reaction heterogeneity at late discharge. The other factor giving rise to a heterogeneous η_{act} is the in-plane variation of μ_p (up to ±0.01 V), which is significantly affected by the local porosity, tortuosity, particle shape and orientation. Due to the high electronic conductivity, μ_e is evenly distributed across the electrode (Fig. 6h) and does not contribute to the heterogeneous reaction. However, cell performance could be affected by the inhomogeneous electronic conducting phase either due to the CBD distribution (particularly in high mass loading and thick electrodes[6,7]) or from the isolated active materials after fracture[45].

In comparison, the inter- and intra-particle SoL distribution is more uniform after artificially enhancing the solid-state diffusion rate (Ds_f, Fig. 6b). The alleviation of Li saturation at the particle outer surface is conducive to a more homogeneous reaction activity and thus a globally lower η_{act} compared to the original electrode (Fig. 6d). Furthermore, the alleviated Li accumulation contributes to a higher V_{eq} at the reaction interface (Fig. 6k), which suppresses the polarisation from solid-state diffusion and accounts for the higher voltage in Fig. 6g. Notably, enhancing the reaction kinetics (Rk_f) has much less impact on the cell performance than increasing the rate of solid-state diffusion (Ds_f). Although η_{act} is significantly lower than that of Ds_f (Fig. 6f), the slow solid-state diffusion renders an identical SoL distribution with the original electrode, leading to a much lower V_{eq} (Fig. 6j) and thus a decreased μ_e compared to Ds_f, especially at the end of discharge (Fig. 6g).

These findings substantiate our conclusion that, for uncalendered NMC electrodes with a mass loading 90 – 94 wt% and an initial thickness less than 50 μm (AM_L and AM_LH), Li$^+$ ion transport in the electrolyte is not the predominant factor in determining the electrochemical performance, even when the electrode is calendered up to approx. 23%. It is instead the sluggish solid-state diffusion that causes a high Li concentration at the particle surface and polarises the cell by introducing an early equilibrium state at the particle/electrolyte interface, undermining its high-rate performance, especially for electrodes composed of large particles. The adverse effect of calendering in this electrode specification is associated primarily with the reduced reaction kinetics originating from the drop in porosity. A higher operating temperature or the use of smaller active particles can significantly improve the performance, both in terms of fast reaction kinetics and solid-state diffusion rate, but at the expense of safety and energy density. Crystallites orientations of the primary particles that consist of the secondary NMC particle also can considerably facilitate solid-state mass transport[46] and prohibit intra-particle crack formation[47,48] that would otherwise make it more sluggish.

Disordered arrangement of excessive lithium and transition metal in rocksalt crystalline structure has been proved to be another option to improve the lithium transport property[49].
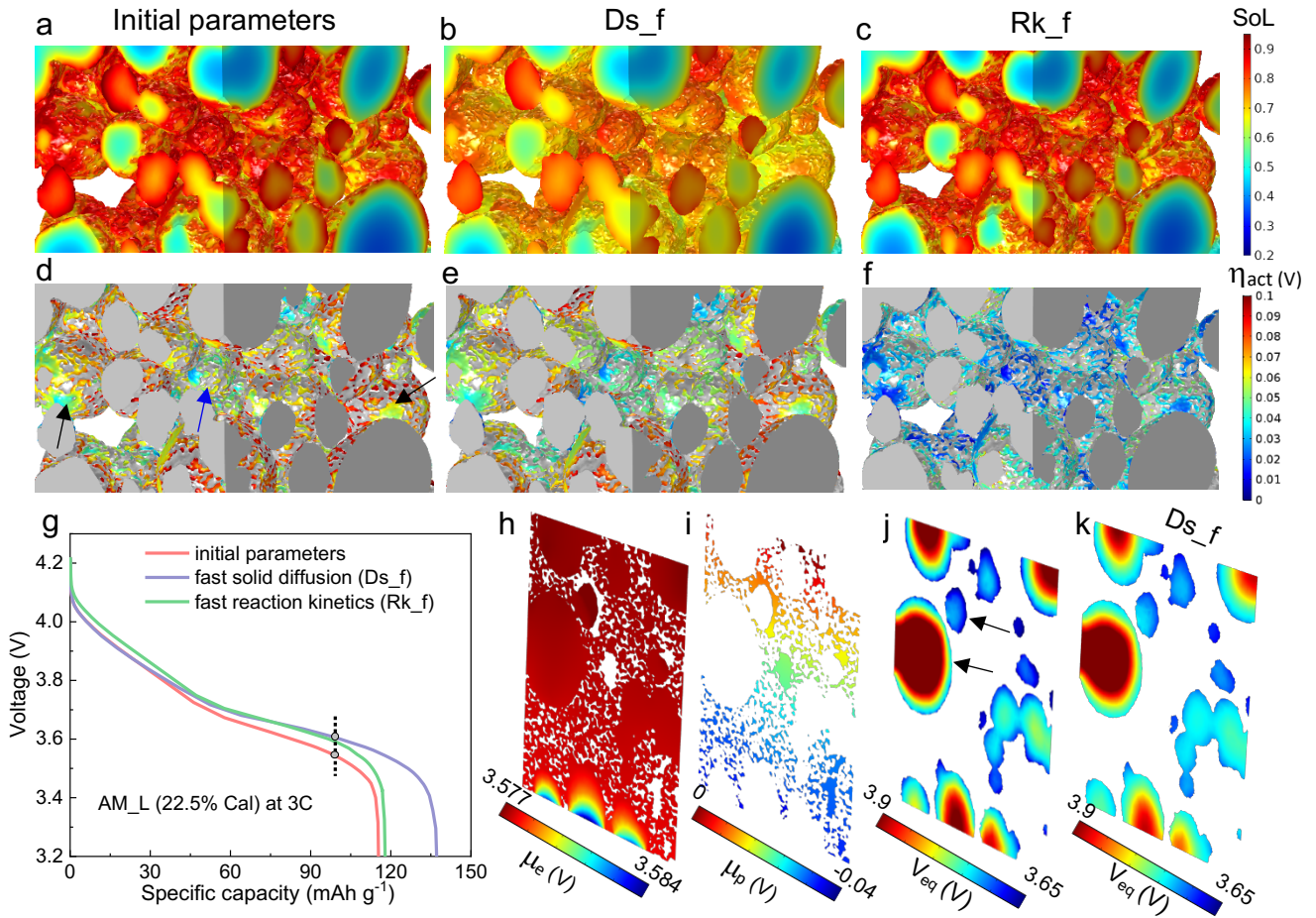

Fig. 6 Evaluating the effect of solid-state diffusion and reaction kinetics in determining the discharge performance of AM_L. (a)-(c) and (d)-(f) Spatial distribution of SoL and η_{act} at 60% DoD, 3C discharge in AM_L, corresponding to the time step highlighted by the black dashed line in (g), which compares the discharge curves simulated at 3C; (h)-(k) the transient potential in the electron conducting phase μ_e, in ion conducting phase μ_p, equilibrium potential V_{eq} and V_{eq} under faster solid-state diffusion, corresponding to the time step highlighted in (g). Black and blue arrows in (d) indicate the low η_{act} arising from locally large pore and small particles respectively. Black arrows in (j) compare the marked difference of V_{eq} at the surface of small and large particles, leading to heterogeneous performance.

Microstructure optimisation of electrode by calendering

Electrode calendering, in essence, tailors the microstructure by changing the combination of electrode thickness and porosity to meet the power and energy density requirement for different applications. Hence, it is crucial to determine the transition point at which mass transport in the electrolyte becomes dominant in cell performance, by taking into account electrode geometries of increased thickness at different porosities, to provide further insights into microstructure design and optimisation. Fig. 7a compares the rated capacity for the uncalendered and heavily calendered AM_L (22.5%) and AM_S (24%) with increasing electrode thickness, which is achieved by virtually mirroring the initial electrode in the thickness direction. The electrode thickness hence becomes the only variable, while the rest of the microstructural parameters (listed in Table 1) are maintained constant (e.g. porosity, particle size distribution, volume fraction, etc). AM_S plots show that increasing the thickness of the electrode by 150% (AM_S1.5) only slightly affects the performance until reaching 3C, where a capacity drop is more visible. Doubling the thickness to 70 μm (AM_S2) yields a comparable capacity loss to AM_S1.5 (red and orange arrows in Fig. 7a), implying a linear dependence for such electrode geometry. Furthermore, it is noted that calendering to 24 % does not affect the rated capacity coμparably to increasing thickness, indicating that surface reaction kinetics do not play a critical role in determining the rate performance of AM_S electrodes.

In contrast, a stronger response to calendering and electrode thickness is seen in the AM_L plots. Due to the lower specific reaction area, calendering is more influential. More importantly, a non-linear capacity drop (blue and vanilla

colour arrows in Fig. 7a) with incremental electrode thickness is found, indicating the increasing importance of Li$^+$ ion transport in determining the performance. The influence of electrode thickness on the performance is unravelled by spatial visualisation of the SoL and C_{ey} distribution in Fig. 7b and c for AM_S and AM_L respectively. The SoL changes from a homogeneous to a preferential distribution in the vicinity of the separator in AM_S. Based on the detailed micro-dynamics analysis in the last section, this results from higher reaction kinetics due to the higher local electrolyte concentration, highlighted by the C_{ey} distribution. C_{ey} decreases linearly from 600, 500 to 400 mol m^{-3} at the current collector for AM_S, AM_S1.5 and AM_S2 respectively. At the end of discharge (83% DoD), AM_S2 displays a more significant preferential lithiation adjacent to the separator and a steeper gradient of C_{ey}, with the lowest value falling below 200 mol m^{-3} at the current collector, indicating significant electrolyte depletion. Compared with AM_S electrodes, AM_L electrodes (Fig. 7c) present a distinct SoL distribution but a similar C_{ey} distribution. An SoL gradient is developed in AM_L as well but to a lesser degree compared to the AM_S electrodes, as solid-state diffusion is the rate-limiting step.

At the end of discharge (67% DoD), a significant amount of active material remains unutilised, which is in sharp contrast to AM_S2 (end). The C_{ey} is less depleted in AM_L2 (end) as a consequence of early stop. This implies that, when the heavily calendered (above 20%) electrode thickness is doubled, the performance of the electrode comprising of small particles is mainly determined by Li$^+$ ion transport. On the other hand, in electrodes comprised of coarse particles, both solid-state diffusion and Li$^+$ ion transport play important roles in determining the rate capability, whereas the polarisation arising from solid-state diffusion, which aggravates with continuing insertion of Li flux, becomes dominant towards the end of discharge. This provides meaningful insights into microstructural design and optimisation for practical applications: for power-oriented design, 80% of the total capacity can be maintained at 3C after calendering an AM_S cathode coating from 87 to 66 μm (24%). A higher C-rate or heavier calendering will exacerbate the performance drop unless an electrolyte with a higher transference number or improved diffusion coefficient is used. Although solid-state diffusion is the primary factor determining the performance of electrodes composed of large particles, the downside of increasing the electrode thickness is that the increased capacity cannot be fully utilised by the additional active material due to the higher current that further aggravates the solid-state diffusion polarisation. This explains why a high areal mass loading (mAh cm^{-2}) electrode often has a lower capacity than a low areal mass loading electrode, particularly at high C-rates.

To assist the microstructural design of the electrode for specific applications, it is not informative to suggest an optimal areal or gravimetric mass loading (g cm^{-2}) that in reality can be achieved by different combinations of porosity and thickness. Thus Fig. 7d is mapped to show the dependence of rated specific capacity on the dual-variation of both porosity and thickness at 3C discharge. Different thickness electrodes are obtained by virtually mirroring and/or cropping the existing electrodes of three different porosities, for AM_L and AM_S respectively. The colourmap, combined with the contour, indicate that the rated capacity of AM_S electrodes decreases monotonically along the diagonal direction, implying that the thickness and porosity play an equivalently important role in determining the capacity. For AM_L electrodes, a two-stage trend is observed: the performance drops slowly with a linear dependence on the electrode thickness up to 70 μm when the porosity is above 0.25. A similar relationship is seen between the capacity and porosity from 0.32 to 0.25 across the whole range of electrode thickness. This implies that porosity plays a vital role in maintaining the specific capacity in AM_L electrodes and 0.25 can be regarded as a transition point, above which the electrode thickness is not particularly influential, compared to the region below 0.25, where a catastrophic performance decrease is observed. This affects thinner electrodes less than the thicker ones, evidenced by the difference in slope. Furthermore, electrodes with higher porosity are less susceptible to the drawbacks of increased thickness in this region. The large difference in z-axis between AM_L and AM_S is primarily attributed to the polarisation from solid-state diffusion. The higher specific reaction area and fast solid-state diffusion make the performance more robust against the structural change associated with calendering. As for AM_L, high porosity can compensate for the disadvantage of sluggish solid-state diffusion and slow reaction kinetics, and thus a thicker electrode can be manfactured without significant performance loss. Drastic capacity loss in low porosity AM_L is a joint effect of the exacerbated polarisation of solid-state diffusion[50] and slower reaction kinetics induced by calendering. Despite delineating the link between microstructure and performance at 3C discharge, Fig. 7 is expected to provide a insightful reference for electrode design and optimisation from composition refinement to the subsequent calendering control.
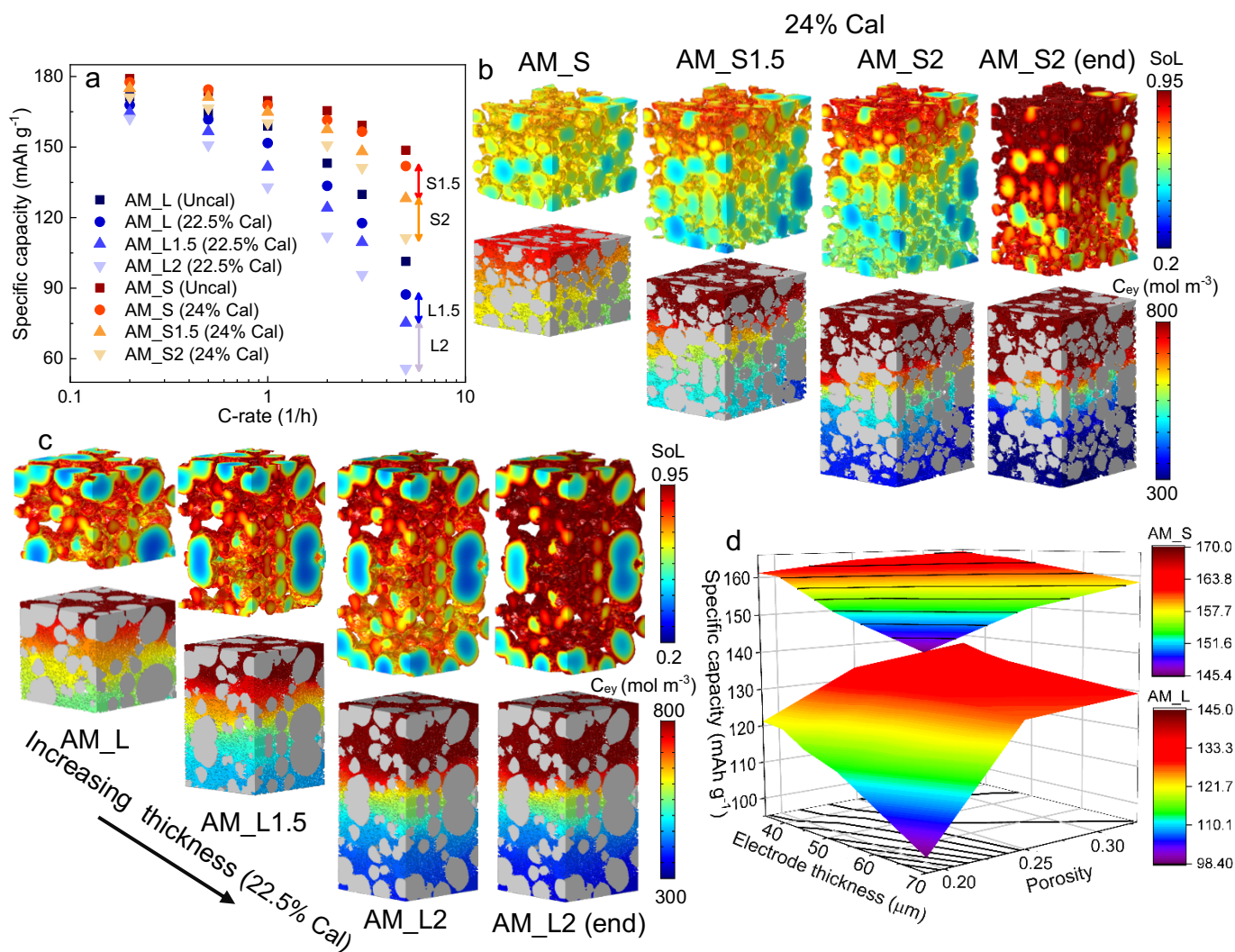
Fig. 7 Overview of the cell performance obtained from electrodes with incremental thickness and calendering ratio. (a) Comparison of the simulated rated specific capacity of uncalendered, calendered and increasing thickness of calendered AM_L and AM_S electrodes; (b) and (c) SoL and C_{ey} distribution at 60% DoD (first three columns) and end of discharge (last column; 67% DoD for AM_L and 83% DoD for AM_S) for heavily calendered AM_S and AM_L electrodes, respectively; (d) dependence of specific capacity on the bi-variation of porosity and electrode thickness for AM_S and AM_L electrodes. Electrochemical performance in (b), (c) and (d) is obtained at 3C discharge.

To further corroborate the conclusion above, three electrodes of increasing thicknesses and thereby areal capacities were prepared and compared with the ones calendered to ca. 20% (Fig. 8). By comparing the uncalendered 1mAh cm^{-2} and 2mAh cm^{-2} discharge curves (Fig. 8a and c) with the calendered ones (Fig. 8b and d), it is found that the curve shapes are almost identical, even at 5C, which is consistent with the previous observation that electrolyte transport does not limit the performance, whereas the 2mAh cm^{-2} electrode exhibits more pronounced capacity loss as the C-rate increases, due to the larger lithiating current and thus an exacerbated solid-state diffusion polarisation. It is noted that the discharge curves of both electrodes globally shifted towards the left compared to the uncalendered ones even at 0.2C, consistent with the prediction in Fig. 8. As explained earlier, this is likely due to the loss of reacting interfacial area after calendering.

Calendering a thin electrode (ca. 2 to 3 times of the particle size) has a higher chance to generate cracks between the CBD and active material particle surface, undermining the electronic percolation and reaction homogeneity. The thick electrode (3mAh cm^{-2}) shows the highest susceptibility of rated capacity to calendering, due to the combined effect of solid-state diffusion and electrolyte transport, as is shown in Fig. 7. The rated capacity of the calendered 3 mAh cm^{-2} electrode (Fig. 8f) is within 10% variation compared to the predicted values for AM_L2 in Fig. 7a. A noticeably lower initial capacity is observed in Fig. 8e, possibly due to the bad electronic conducting percolation that is a known issue in thick and high mass loading electrodes[6]. However, calendering favoured its capacity retention at low C-rate by

densifying the structure, which agrees with the previous study[6,51], but the drastic capacity drop beyond 1C suggests that this type of electrode is only appropriate for energy density-oriented applications, unless operating at higher temperature and/or fabricating the crystallites to align in the radial direction of the secondary particle. Despite the unfavoured power capability, AM_L is superior to AM_S in the aspect of long-term durability due to less side reactions and safer as the temperature rises[52,53]. Furthermore, the gravimetric capacity assessed in this study highlights the utilisation of the active material under calendering, however, the volumetric capacity always increases with incremental calendering.
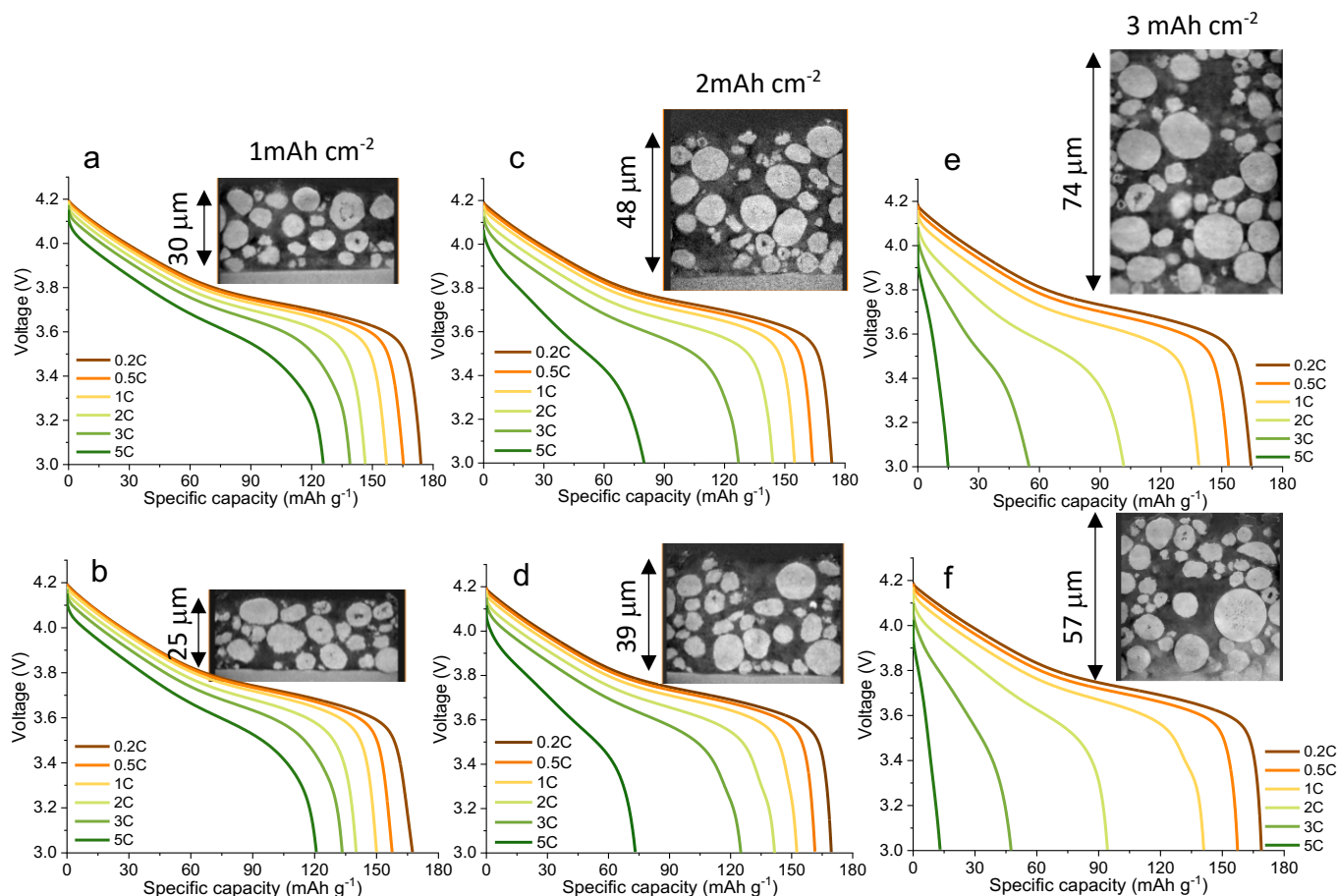

Fig. 8 Comparison of the discharge performance by experiment between electrodes of different mass loadings before and after calendering.

Conclusion

In this study, we investigated the different microstructural evolution of NMC cathodes composed of large and small active material particles respectively, under incremental calendering and its consequential influence on electrochemical performance, using combined in-situ X-ray nano-computed tomography, image-based battery modelling and experiment.

Results show that electrodes composed of large particles with broad size distribution (AM_L, D_{mean} = 7.3 ± 3.1 μm, C_{50} = 3C and C_{90} = 0.8C) present large microstructural heterogeneity that leads to spatial self-arrangement during calendering, such as inter-particle rotation, uneven deformation and a loss of pore connectivity. In contrast, electrodes comprised of small particles (AM_S, D_{mean} = 5.2 ± 1.8 μm, C_{50} = 5C and C_{90} = 1.8C) are structurally stable with homogeneous deformation and a lower pore tortuosity under calendering. The rated specific capacity is much higher in AM_S and is less affected by the porosity loss due to calendering densification.

For an uncalendered electrode with an initial thickness of 50 μm, Li$^+$ ion transport does not significantly affect the high-rate performance (up to 5C) and it is the solid-state diffusion that predominantly determines the performance, especially for AM_L that has a longer diffusion path. Almost 80% of initial capacity can be retained for a 66 μm thick AM_S electrode after 24% calendering at 3C discharge. Performance drop is observed exponentially with the increase

of electrode thickness for AM_L, especially when the thickness is above 50 µm. Calendering exacerbates reaction heterogeneity in AM_L, leading to further underutilisation of the active material, whereas it does not affect the uniform lithiation in AM_S. By exploring the dependence of performance on the dual-variation of electrode thickness and porosity, insights into electrode design and microstructural optimisation are obtained; thickness and porosity play equivalent roles in determining the rated capacity of AM_S; as for AM_L, a porosity of 0.25 can be regarded as a transition point, above which the performance of the electrode is governed by both the porosity and thickness just as AM_S, otherwise a catastrophic drop in performance is inevitable as the electrode gets thicker. These results help to provide quantitative insight into electrode optimisation.

Experimental Section

Materials

Uncalendered and 18% calendered $LiNi_{0.6}Mn_{0.2}Co_{0.2}O_2$ (NMC 622) cathodes (AM_LH) with a mass loading of 130 g m^{-2} manufactured by AGM Batteries Ltd (UK) were used in this study to develop and validate the model. The ratio of active material (BASF, Germany), conductive carbon (C65, KS6L 2:1) and binder (PVDF, Solref) was 94.5:3:2.5. The aluminium current collector was 15 µm thick. A Swagelok half-cells (PFA, Swagelok, UK) were assembled with NMC 622 as the positive electrode (12 µµ diameter), lithium metal as the negative electrode (12 mm diameter), and Celgard 2325 separator (12.8 mm) as the separator. 50 µL of 1M $LiPF_6$ in EC/EMC (3:7 v/v) + 1wt% vinylene carbonate (VC, Soulbrain, USA) was used as the electrolyte. AM_L and AM_S were prepared using the $LiNi_{0.33}Mn_{0.33}Co_{0.33}O_2$ powders manufactured by MTI (USA) and Targray (Canada) respectively. 90:5:5 mass ratio of the active material, conductive carbon (Super C65, Imerys, UK) and Polyvinylidene fluoride (PVDF, Arkema, France) were mixed in an asymmetric centrifuge system (SpeedMixer DAC 150.1 FVZ-K). The slurry was then coated onto a 20 µm thick aluminium current collector and spread using a doctor blade with a 175 µm gap. The electrode sheet was then dried in a vacuum oven overnight at 80 °C. The stand-alone CBD sample was prepared by mixing 50:50 conductive carbon and PVDF with NMP as the solvent, followed by coating and drying at the same temperature[28].

Electrochemical performance test

After the assembly of the Swagelok cell, a formation step composed of two C/10 CC-CV charge (C/100 cut-off) and C/10 CC discharge cycles was conducted within the voltage window 4.2 to 3 V. Electrochemical testing was carried out on VMP3 potentiostats or BCS battery cyclers (Biologic, France). The OCV of NMC622 vs. Li/Li$^+$ was obtained using the Galvanostatic Intermittent Titration Technique (GITT, Figure S9). The cells were discharged and charged at a constant current corresponding to a C-rate of C/10 in steps of 2.5% state of charge, followed by a pause at open circuit for 5 hours to allow the voltage to relax prior to OCV measurement. This pulse/relaxation cycle was repeated until reaching the cut-off voltage (3V and 4.2 V for discharge and charge respectively). The solid-state diffusion coefficient was obtained from the GITT data by following a method described previously[54].

X-ray nano-computed tomography and in-situ compression

The uncalendered AM_L and AM_S were initially punched into a 1 mm disk from the electrode sheet and glued onto the tip of a pin by epoxy, followed by laser milling that targeted the final pillar size below 90 µm in diameter to ensure sufficient X-ray transmission and signal-to-noise ratio[55]. The prepared electrodes were mounted on a nano-mechanical test stage developed for integration into the Zeiss Xradia Ultra 810 X-ray microscope[56] (Carl Zeiss, CA, USA) (Fig. 1a and b). A flat-headed stainless-steel pin, attached to a piezo-mechanical actuator, was used to compress the electrode. The whole assembly was mounted on the sample stage, which rotates for tomographic data collection. The placement of capillary condenser and zone plate in the beam path helps to produce a quasi-monochromatic parallel beam with an energy of 5.4 keV, achieving a voxel size of 64 nm (i.e. camera binning 1), corresponding to a field of view of 64 µm × 64 µm^2. 1201 radiographic projections were sequentially collected at an exposure time of 60 seconds over 144° rotation of the pillars. A standard filtered back-projection algorithm[57] were used for the 3D reconstruction, which was then imported into the commercial software package Avizo V9.5 (Avizo, Thermo Fisher Scientific, Waltham, Massachusetts, U.S.) for post analysis. The same procedure was repeated for the stand-alone CBD sample. The electrodes calendered by the test stage and by a roller calendering machine are compared in Figure S10. The measured material parameters are within 8% of difference (Table S3).

Dual-scan superimposition (DSS) technique

To reconstruct the full microstructure of the NMC electrode, a novel dual-scan superimposition technique has been developed as described elsewhere[27] to resolve the low-absorption carbon-binder and nano-pore phases: the NMC electrode and the stand-alone carbon-binder phase were scanned separately using the same parameters. The active particles and macro-pores that have good contrast were segmented in the full electrode scan, whereas the blurred carbon-binder phase was then replaced by the second scan of higher contrast-to-noise ratio. Before further microstructural characterisation, the reconstructed grayscale 3D electrode was first segmented into active material, carbon-binder and pore phases using thresholding techniques in Avizo 9.5, with the FWHM (50% contrast) criterion used to determine the phase boundary (Figure S11-S12). The tortuosity factor was obtained by the open-source software TauFactor[58]. The permeability simulation was conducted in Avizo XLab package, by assigning a pressure difference (permeability is independent of the magnitude of the pressure gradient) to the pore phase at the inlet and outlet with a non-slip boundary condition.

Representative volume element (RVE) analysis and measurement deviations

Key material parameters of the uncalendered AM_L electrode are measured and compared using nano-CT data and micro-CT data (much larger sample) respectively (Figure S13). The particle size distribution agrees well between the two cases, with little disparity of NMC volume fraction and mean diameter of the particle (4.7% difference). In addition, representative volume element analysis on the nano-CT sample is presented in Figure S14, by measuring the porosity and tortuosity as a function of the incrementally dilated volume fraction of the electrode (from 10% to 100% of the sample size). Moreover, two additional uncalendered AM_L electrodes of the similar size are characterised quantitatively to highlight the sample-tosample variation (Figure S15). Finally, the key material parameters obtained from sample 2 and sample 3 are compared with sample 1 (used in this study) in Table S4, with standard deviation given.

3D physics-based microstructure-resolved model

The 3D electrode volumes were first segmented into NMC particles, carbon-binder and pore according to the different grayscale values, followed by adaptive meshing in the commercial software Simpleware ScanIP N-2018.03.

The generalised Poisson-Nernst-Planck (gPNP) mathematic model[59], which originated from the Newman battery model[60], was employed with concentrated solution theory[59,61], by assigning partial differential governing equations (PDEs) to electrolyte (pore), NMC particles and CBD individually in COMSOL Multiphysics V5.5. Solid-state and electron transport were described by Fick's law and Ohm's law respectively. The Butler-Volmer equation was used for the charge transfer reaction, with the exchange current density associated with the concentration of the reactants in the electrolyte and active material. Details of the physical equations, boundary conditions and input parameters are shown in the Supplementary Information. No volume-averaged material parameters, such as porosity, tortuosity and particle size were used in the microstructure-resolved model.

Supplemental Information

Supplementary Information include 15 figures and 4 tables can be found with the manuscript submission.

Acknowledgements

Author contributions

X.L. and P.R.S. conceived the study. X.L., S.R.D. and L.R. conducted the *in situ* X-ray CT scans and image analysis. X.L. and A.B. conducted the modelling. M.D.R.K. helped with the python coding. K.B.O. and E.K. performed the rate capability test of the calendered cells. X.L. drafted the manuscript and A.B., S.R.D., L.R., M.D.R.K, J.P., K.B.O., G.H., E.K., D.JR.B. and P.R.S. reviewed the manuscript.

Declaration of interests

The authors declare no competing interests.

References

1. Gröger, O., Gasteiger, H.A., and Suchsland, J.-P. (2015). Review—Electromobility: Batteries or Fuel Cells? Journal of The Electrochemical Society *162*, A2605-A2622.

2. Xu, Y., Hu, E., Zhang, K., Wang, X., Borzenets, V., Sun, Z., Pianetta, P., Yu, X., Liu, Y., and Yang, X.-Q. (2017). In situ visualization of state-of-charge heterogeneity within a LiCoO2 particle that evolves upon cycling at different rates. ACS Energy Letters *2*, 1240-1245.

3. Harris, S.J., and Lu, P. (2013). Effects of Inhomogeneities   Nanoscale to Mesoscale   on the Durability of Li-Ion Batteries. The Journal of Physical Chemistry C *117*, 6481-6492.

4. Finegan, D.P., Scheel, M., Robinson, J.B., Tjaden, B., Hunt, I., Mason, T.J., Millichamp, J., Di Michiel, M., Offer, G.J., Hinds, G.*, et al.* (2015). In-operando high-speed tomography of lithium-ion batteries during thermal runaway. Nature Communications *6*, 6924.

5. Kwade, A., Haselrieder, W., Leithoff, R., Modlinger, A., Dietrich, F., and Droeder, K. (2018). Current status and challenges for automotive battery production technologies. Nature Energy *3*, 290-300.

6. Lenze, G., Röder, F., Bockholt, H., Haselrieder, W., Kwade, A., and Krewer, U. (2017). Simulation-Supported Analysis of Calendering Impacts on the Performance of Lithium-Ion-Batteries. *164*, A1223-A1233.

7. Zheng, H., Tan, L., Liu, G., Song, X., and Battaglia, V.S. (2012). Calendering effects on the physical and electrochemical properties of Li[Ni1/3Mn1/3Co1/3]O2 cathode. Journal of Power Sources *208*, 52-57.

8. Davoodabadi, A., Li, J., Liang, Y., Wood, D.L., Singler, T.J., and Jin, C. (2019). Analysis of electrolyte imbibition through lithium-ion battery electrodes. Journal of Power Sources *424*, 193-203.

9. Davoodabadi, A., Li, J., Liang, Y., Wang, R., Zhou, H., Wood, David L., Singler, T.J., and Jin, C. (2018). Characterization of Surface Free Energy of Composite Electrodes for Lithium-Ion Batteries. Journal of The Electrochemical Society *165*, A2493-A2501.

10. Haselrieder, W., Ivanov, S., Christen, D., Bockholt, H., and Kwade, A. (2013). Impact of the Calendering Process on the Interfacial Structure and the Related Electrochemical Performance of Secondary Lithium-Ion Batteries. ECS Transactions *50*, 59-70.

11. Sheng, Y., Fell, C.R., Son, Y.K., Metz, B.M., Jiang, J., and Church, B.C.J.F.i.E.R. (2014). Effect of calendering on electrode wettability in lithium-ion batteries. *2*, 56.

12. Meyer, C., Kosfeld, M., Haselrieder, W., and Kwade, A. (2018). Process modeling of the electrode calendering of lithium-ion batteries regarding variation of cathode active materials and mass loadings. Journal of Energy Storage *18*, 371-379.

13. Meyer, C., Bockholt, H., Haselrieder, W., and Kwade, A. (2017). Characterization of the calendering process for compaction of electrodes for lithium-ion batteries. Journal of Materials Processing Technology *249*, 172-178.

14. Gallagher, K.G., Trask, S.E., Bauer, C., Woehrle, T., Lux, S.F., Tschech, M., Lamp, P., Polzin, B.J., Ha, S., Long, B.*, et al.* (2015). Optimizing Areal Capacities through Understanding the Limitations of Lithium-Ion Electrodes. Journal of The Electrochemical Society *163*, A138-A149.

15. Shearing, P.R., Howard, L.E., Jørgensen, P.S., Brandon, N.P., and Harris, S.J. (2010). Characterization of the 3-dimensional microstructure of a graphite negative electrode from a Li-ion battery. Electrochemistry communications *12*, 374-377.

16. Otagawa, T., Jina, A.N., and Madou, M.J. (1994). Three-dimensional microstructure as a substrate for a battery electrode (Google Patents).

17. Stephenson, D.E., Walker, B.C., Skelton, C.B., Gorzkowski, E.P., Rowenhorst, D.J., and Wheeler, D.R. (2011). Modeling 3D microstructure and ion transport in porous Li-ion battery electrodes. Journal of The Electrochemical Society *158*, A781-A789.

18. Günther, T., Schreiner, D., Metkar, A., Meyer, C., Kwade, A., and Reinhart, G.J.E.T. (2020). Classification of Calendering‐Induced Electrode Defects and Their Influence on Subsequent Processes of Lithium‐Ion Battery Production. *8*, 1900026.

19. Sangrós Giménez, C., Finke, B., Schilde, C., Froböse, L., and Kwade, A. (2019). Numerical simulation of the behavior of lithium-ion battery electrodes during the calendaring process via the discrete element method. Powder Technology *349*, 1-11.

20. Mistry, A.N., Smith, K., Mukherjee, P.P.J.A.a.m., and interfaces (2018). Secondary-phase stochastics in lithium-ion battery electrodes. *10*, 6317-6326.

21. Zielke, L., Hutzenlaub, T., Wheeler, D.R., Manke, I., Arlt, T., Paust, N., Zengerle, R., and Thiele, S.J.A.E.M. (2014). A Combination of X‐Ray Tomography and Carbon Binder Modeling: Reconstructing the Three Phases of LiCoO2 Li‐Ion Battery Cathodes. *4*, 1301617.

22. Taiwo, O.O., Finegan, D.P., Eastwood, D.S., Fife, J.L., Brown, L.D., Darr, J.A., Lee, P.D., Brett, D.J., and Shearing, P.R. (2016). Comparison of three‐dimensional analysis and stereological techniques for quantifying lithium‐ion battery electrode microstructures. Journal of microscopy *263*, 280-292.

23. Finegan, D.P., Cooper, S.J., Tjaden, B., Taiwo, O.O., Gelb, J., Hinds, G., Brett, D.J., and Shearing, P.R. (2016). Characterising the structural properties of polymer separators for lithium-ion batteries in 3D using phase contrast X-ray microscopy. Journal of Power Sources *333*, 184-192.

24. Trembacki, B.L., Mistry, A.N., Noble, D.R., Ferraro, M.E., Mukherjee, P.P., and Roberts, S.A. (2018). Editors' Choice—Mesoscale Analysis of Conductive Binder Domain Morphology in Lithium-Ion Battery Electrodes. Journal of The Electrochemical Society *165*, E725-E736.

25. Zielke, L., Hutzenlaub, T., Wheeler, D.R., Manke, I., Arlt, T., Paust, N., Zengerle, R., and Thiele, S. (2014). A Combination of X‐Ray Tomography and Carbon Binder Modeling: Reconstructing the Three Phases of LiCoO2 Li‐Ion Battery Cathodes. Advanced Energy Materials *4*, 1301617.

26. Mistry, A.N., Smith, K., and Mukherjee, P.P. (2018). Secondary-Phase Stochastics in Lithium-Ion Battery Electrodes. ACS applied materials & interfaces *10*, 6317-6326.

27. Lu, X., Bertei, A., Finegan, D.P., Tan, C., Daemi, S.R., Weaving, J.S., O'Regan, K.B., Heenan, T.M.M., Hinds, G., Kendrick, E.*, et al.* (2020). 3D microstructure design of lithium-ion battery electrodes assisted by X-ray nano-computed tomography and modelling. Nature Communications *11*, 2079.

28. Daemi, S.R., Tan, C., Volkenandt, T., Cooper, S.J., Palacios-Padros, A., Cookson, J., Brett, D.J.L., and Shearing, P.R. (2018). Visualizing the Carbon Binder Phase of Battery Electrodes in Three Dimensions. ACS Applied Energy Materials *1*, 3702-3710.

29. Usseglio-Viretta, F.L., Colclasure, A., Mistry, A.N., Claver, K.P.Y., Pouraghajan, F., Finegan, D.P., Heenan, T.M., Abraham, D., Mukherjee, P.P., and Wheeler, D.J.J.o.T.E.S. (2018). Resolving the discrepancy in tortuosity factor estimation for Li-ion battery electrodes through micro-macro modeling and experiment. *165*, A3403-A3426.

30. Landesfeind, J., Hattendorff, J., Ehrl, A., Wall, W.A., and Gasteiger, H.A.J.J.o.T.E.S. (2016). Tortuosity determination of battery electrodes and separators by impedance spectroscopy. *163*, A1373-A1387.

31. Chung, D.-W., Shearing, P.R., Brandon, N.P., Harris, S.J., and García, R.E.J.J.o.T.E.S. (2014). Particle size polydispersity in Li-ion batteries. *161*, A422-A430.

32. Ebner, M., Chung, D.W., García, R.E., and Wood, V.J.A.E.M. (2014). Tortuosity anisotropy in lithium‐ion battery electrodes. *4*, 1301278.

33. Hu, X., Li, S., and Peng, H. (2012). A comparative study of equivalent circuit models for Li-ion batteries. Journal of Power Sources *198*, 359-367.

34. Birkl, C., and Howey, D. (2013). Model identification and parameter estimation for LiFePO4 batteries.

35. Forouzan, M.M., Mazzeo, B.A., and Wheeler, D.R. (2018). Modeling the Effects of Electrode Microstructural Heterogeneities on Li-Ion Battery Performance and Lifetime. Journal of The Electrochemical Society *165*, A2127-A2144.

36. Doyle, M., and Fuentes, Y. (2003). Computer simulations of a lithium-ion polymer battery and implications for higher capacity next-generation battery designs. Journal of The Electrochemical Society *150*, A706-A713.

37. Daemi, S.R., Lu, X., Sykes, D., Behnsen, J., Tan, C., Palacios-Padros, A., Cookson, J., Petrucco, E., Withers, P.J., Brett, D.J.L.*, et al.* (2019). 4D visualisation of in situ nano-compression of Li-ion cathode materials to mimic early stage calendering. Materials Horizons *6*, 612-617.

38. Lu, X., Fernández, M.P., Bradley, R.S., Rawson, S.D., O'Brien, M., Hornberger, B., Leibowitz, M., Tozzi, G., and Withers, P.J. (2019). Anisotropic crack propagation and deformation in dentin observed by four-dimensional X-ray nano-computed tomography. Acta Biomaterialia *96*, 400-411.

39. Zhao, S., Zhang, N., Zhou, X., and Zhang, L. (2017). Particle shape effects on fabric of granular random packing. Powder Technology *310*, 175-186.

40. Doyle, M., Fuller, T.F., and Newman, J.J.J.o.t.E.s. (1993). Modeling of galvanostatic charge and discharge of the lithium/polymer/insertion cell. *140*, 1526.

41. Tsai, P.-C., Wen, B., Wolfman, M., Choe, M.-J., Pan, M.S., Su, L., Thornton, K., Cabana, J., and Chiang, Y.-M. (2018). Single-particle measurements of electrochemical kinetics in NMC and NCA cathodes for Li-ion batteries. Energy & Environmental Science *11*, 860-871.

42. Xia, Y., Zheng, J., Wang, C., and Gu, M. (2018). Designing principle for Ni-rich cathode materials with high energy density for practical applications. Nano Energy *49*, 434-452.

43. Hendricks, C., Williard, N., Mathew, S., and Pecht, M. (2015). A failure modes, mechanisms, and effects analysis (FMMEA) of lithium-ion batteries. Journal of Power Sources *297*, 113-120.

44. Birkl, C.R., Roberts, M.R., McTurk, E., Bruce, P.G., and Howey, D.A. (2017). Degradation diagnostics for lithium ion cells. Journal of Power Sources *341*, 373-386.

45. Xu, R., Sun, H., de Vasconcelos, L.S., and Zhao, K.J.J.o.T.E.S. (2017). Mechanical and structural degradation of LiNixMnyCozO2 cathode in Li-ion batteries: an experimental study. *164*, A3333-A3341.

46. Xu, Z., Jiang, Z., Kuai, C., Xu, R., Qin, C., Zhang, Y., Rahman, M.M., Wei, C., Nordlund, D., Sun, C.-J.*, et al.* (2020). Charge distribution guided by grain crystallographic orientations in polycrystalline battery materials. Nature Communications *11*, 83.

47. Lee, J.H., Yoon, C.S., Hwang, J.-Y., Kim, S.-J., Maglia, F., Lamp, P., Myung, S.-T., and Sun, Y.-K. (2016). High-energy-density lithium-ion battery using a carbon-nanotube–Si composite anode and a compositionally graded Li[Ni0.85Co0.05Mn0.10]O2 cathode. Energy & Environmental Science *9*, 2152-2158.

48. Yan, P., Zheng, J., Gu, M., Xiao, J., Zhang, J.-G., and Wang, C.-M. (2017). Intragranular cracking as a critical barrier for high-voltage usage of layer-structured cathode for lithium-ion batteries. Nature Communications *8*, 14101.

49. Clément, R.J., Lun, Z., and Ceder, G. (2020). Cation-disordered rocksalt transition metal oxides and oxyfluorides for high energy lithium-ion cathodes. Energy & Environmental Science *13*, 345-373.

50. Du, Z., Wood, D.L., Daniel, C., Kalnaus, S., and Li, J. (2017). Understanding limiting factors in thick electrode performance as applied to high energy density Li-ion batteries. Journal of Applied Electrochemistry *47*, 405-415.

51. Smekens, J., Gopalakrishnan, R., Steen, N.V.d., Omar, N., Hegazy, O., Hubin, A., and Van Mierlo, J.J.E. (2016). Influence of electrode density on the performance of Li-ion batteries: Experimental and simulation results. *9*, 104.

52. Li, J., Shunmugasundaram, R., Doig, R., and Dahn, J.R. (2016). In Situ X-ray Diffraction Study of Layered Li–Ni–Mn–Co Oxides: Effect of Particle Size and Structural Stability of Core–Shell Materials. Chemistry of Materials *28*, 162-171.

53. Li, T., Yuan, X.-Z., Zhang, L., Song, D., Shi, K., and Bock, C. (2020). Degradation Mechanisms and Mitigation Strategies of Nickel-Rich NMC-Based Lithium-Ion Batteries. Electrochemical Energy Reviews *3*, 43-80.

54. Chen, C.-H., Brosa Planella, F., O'Regan, K., Gastol, D., Widanage, W.D., and Kendrick, E. (2020). Development of Experimental Techniques for Parameterization of Multi-scale Lithium-ion Battery Models. Journal of The Electrochemical Society *167*, 080534.

55. Bailey, J., Heenan, T., Finegan, D., Lu, X., Daemi, S., Iacoviello, F., Backeberg, N., Taiwo, O., Brett, D., and Atkinson, A.J.J.o.m. (2017). Laser‐preparation of geometrically optimised samples for X‐ray nano‐CT. *267*, 384-396.

56. Schurch, R., Rowland, S.M., Bradley, R.S., and Withers, P.J. (2015). Comparison and combination of imaging techniques for three dimensional analysis of electrical trees. IEEE Transactions on Dielectrics and Electrical Insulation *22*, 709-719.

57. Singh, S., Kalra, M.K., Hsieh, J., Licato, P.E., Do, S., Pien, H.H., and Blake, M.A. (2010). Abdominal CT: comparison of adaptive statistical iterative and filtered back projection reconstruction techniques. Radiology *257*, 373-383.

58. Cooper, S., Bertei, A., Shearing, P., Kilner, J., and Brandon, N.J.S. (2016). TauFactor: An open-source application for calculating tortuosity factors from tomographic data. *5*, 203-210.

59. Cai, L., and White, R.E. (2011). Mathematical modeling of a lithium ion battery with thermal effects in COMSOL Inc. Multiphysics (MP) software. J Power Sources *196*, 5985-5989.

60. Doyle, M., Fuller, T.F., and Newman, J. (1993). Modeling of galvanostatic charge and discharge of the lithium/polymer/insertion cell. J Electrochem Soc *140*, 1526-1533.

61. Lai, W., and Ciucci, F. (2011). Mathematical modeling of porous battery electrodes—Revisit of Newman's model. Electrochim Acta *56*, 4369-4377.